Modelling camera viewing angle deviation to improve nearshore video monitoring

Clément Bouvier, Yann Balouin, Bruno Castelle, Robert Holman

Modelling camera viewing angle deviation to improve nearshore video monitoring

Clément Bouvier [1,2,*], Yann Balouin [1], Bruno Castelle [2] and Robert Holman [3]

[1] BRGM, Univ, Montpellier; c.bouvier@brgm.fr; y.balouin@brgm.fr
[2] CNRS, UMR 5805 EPOC, Univ. Bordeaux; clement.bouvier@u-bordeaux.fr; bruno.castelle@u-bordeaux.fr
[3] CEOAS, Oregon State University; holman@coas.oregonstate.edu
[*] Correspondence: clement.bouvier@u-bordeaux.fr

Keywords: Coastal management; video monitoring; image rectification; empirical modelling

Research highlights:

- **The influence of camera viewing angles' deviation on nearshore video monitoring is explored**
- **The environmental parameters controlling camera movements at the video station of Sète, SE France, are identified**
- **Camera viewing angle deviations are simulated using an empirical model significantly reducing the geo-rectification errors**

Abstract:

Video monitoring the nearshore can provide high-frequency remotely-sensed optical information from which morphological changes and hydrodynamic data can be derived. Although overlooked in most of the studies, it is acknowledged that camera viewing angles can substantially vary in time for a variety of reasons, reducing consistently data accuracy. This paper aims to identify the primary environmental parameters controlling camera shifts at the video monitoring station of Sète (SE France) and develops an empirical model to routinely reduce these deviations. Our model simulates camera movements with an excellent skill (BSS = 0.87) and shows that camera viewing angles' deviation is primarily controlled by the position of the sun during sunny days, making it predictable. This study opens new perspective to routinely improve camera geometry of video monitoring systems.

1. Introduction

Appropriately monitoring the nearshore is challenging given that morphological changes cover a wide range of spatial and temporal scales (Larson and Kraus, 1994). Traditional topo-bathymetric measurements are not compatible with this wide range of scales, mostly because of the cost and the practical difficulties to survey the nearshore (Lippmann and Smith, 2009), particularly in the surf zone. Instead, video monitoring can provide high-frequency remotely-sensed optical information from which morphological changes and hydrodynamic data can be derived. Shoreline-sandbar geometry as well as rip channel positions have long been measured with reasonable accuracy using video stations (Alexander and Holman, 2004; Almar et al., 2010; Gallop et al., 2011; Holman et al., 2006; Lippmann and Holman, 1989; Ruessink et al., 2009). By combining the video-measured shoreline position and elevation, video-based techniques show also good accuracy in estimating the complete intertidal bathymetry for steep beaches (Aarninkhof et al., 2003; Osorio et al., 2012).

A more recently used product from video monitoring is pixel time series (Holman and Stanley, 2007), which are now commonly exploited in coastal research for diverse purposes. Pixel time series usually consists in a 17-mn temporal acquisition of high-frequency (2Hz) measured pixel intensities providing more information none easily measurable in-situ so far. Recent developments and analysis of these time-series give access to multiple parameters still hard to obtain on the field. Such improvements concern diverse coastal research applications such as optically measuring the runup (Holland et al., 1995; Holman and Guza, 1984), the wave directional spectrum (Lippmann and Holman, 1991), the longshore currents in the surf zone (Chickadel, 2003), the breaking wave height (Almar et al., 2012) or the nearshore subtidal bathymetry (Holman et al., 2013). These measurement techniques do not require sampling and storage of the entire image but just the pixel intensities at a number of individual locations, or along cross-shore or alongshore transects.

To provide validation of such video data and to further infer time series, each (u, v) pixel coordinate must be transformed into (x, y, z) real world coordinates (Figure 1a, b). To resolve the equation, one of the

most used models is the pinhole model (Faugeras, 1993; Hartley and Zisserman, 2004; Heikkila and Silven, 1997; Holland et al., 1997; Pérez Muñoz et al., 2013), whose calibration is performed by using camera locations (x0, y0, z0), camera intrinsic (details about the sensor, the camera view field and the distortion parameters of the lens) and extrinsic (tilt, roll or azimuth angle) parameters. These last three geometry parameters correspond to the viewing angle of the camera (Figure 2c) and can be computed by a photogrammetric transformation using a number of ground control points of which the real world coordinates have been accurately measured (Holland et al., 1997).

Although overlooked in most of the studies involving video-derived data, it is acknowledged that camera viewing angles can substantially vary in time for a variety of reasons including thermal and wind effects, especially on tall towers (Holman and Stanley, 2007). A relatively small shift in tilt and/or roll on camera orientation can lead to shift in a few pixels and, in turn, in real world coordinates on the order meters to tens of meters, or even more depending on the distance of the area of interest from the camera location. Figures 1a and 1c provide an extreme example at the video monitoring station of Sète, SE France (Bouvier et al., 2017), with a 0.43 ° tilt and a 0.15 ° roll deviation between two images resulting in a large shift in the location, size and shape of the sampling area (colored box on Figure 1d). This error reaches 130 m in the longshore and 20 m in the cross-shore direction for box 2 located approximately 600 m from the camera.

Such movements are likely to occur for a certain number of outdoor installations (Holman and Stanley, 2007; Pearre and Puleo, 2009; Radermacher et al., 2018; Vousdoukas et al., 2011). Thereby, each image requires a specific geometry solution (tilt, roll and azimuth value) calculated after acquisition assuming camera location and intrinsic parameters remain the same.

An accurate geometry solution for one image is usually obtained detecting a certain number of fixed salient points (ground control points) on the camera fields. Although tedious, this systematic geometry rectification is often efficient in providing accurately rectified images. Consequently, the frequency of accurate geo-rectified images usable for nearshore monitoring often reduce drastically (often more than 90 %) depending of the time allowed for the geo-rectification process. Despite attempts to stabilize the

camera-mounting structure at certain video monitoring stations (Pearre and Puleo, 2009), camera movement remain significant constraining the user to elaborate a rectification procedure. Previous efforts to automatically compensate camera movements automatically post-acquisition have been often realized using feature matching (Pearre and Puleo, 2009; Vousdoukas et al., 2011). Such techniques systematically apply a procedure consisting in identifying the deviation of a region of interest, providing the camera viewing angle deviations and then an automatic geo-rectification. Such methods have been further developed with the increased use of drones and became more computationally efficient (Colomina and Molina, 2014; Turner et al., 2016). Such approach can correct high (e.g. induced by the wind) and low frequency (e.g. thermal expansion) camera field movement. However, such a technique requires the presence of fixed salient points (e.g. building, road) or any fixed region with high contrast in the camera view field. If the camera view field essentially consists in the beach and the ocean with no fixed points, which is common in coastal monitoring, camera displacement rectification is not possible and video data are typically taken at face value. The same occurs for scheduled pixel time series acquisitions along a point, a transect or for a grid which can be used, for instance, for depth inversion purposes (Holman et al., 2013). The solution, which would consist in recording each snapshot on which feature matching and geo-rectification would be performed (pending salient fixed points are available), is computationally very expensive and impossible for operational purposes. Therefore, it is crucial to define which environmental variables control the camera movements to further develop generic methods for rectification procedures using time-varying geometry.

This paper aims to identify the primary environmental parameters controlling camera shifts of the Argus station of Sète (SE France) and to propose an empirical model to routinely reduce these deviations after acquisition or even before a scheduled pixel sampling. After a brief description of the video monitoring system of Sète (section 2), the data and method used to unravel the cause of the camera drifts are given in section 3. Results (section 4) are discussed in section 5 before conclusions are drawn in section 6. We show that camera viewing angles deviation is driven by thermal distortion, which make predictable these camera shifts and opens to perspective to routinely improve camera geometry of video

78 monitoring systems.

79

80 **2. Field site**

81 The Lido of Sète, SE France, is a narrow and relatively straight sandy barrier separating the Thau
82 lagoon from the Mediterranean Sea in the northern part of the Gulf of Lion (Figure 2a). A large beach
83 management program was developed to mitigate chronic erosion involving the deployment of a 1-km long
84 submerged breakwater. A permanent video monitoring system was installed in April 2011 to study
85 morphological evolution following this coastal management program (Bouvier et al., 2017).

86 The video monitoring system of Sète consists in 8 cameras mounted on two 20-m high and 2.5-km
87 spaced reinforced concrete mast (Figure 2d). This study focusses on Mast 2, which provides a complete
88 data time series and offers a 180 ° view of the beach with 5 cameras (C1 to C5, Figure 2b) oriented to
89 obtain a panoramic view of the coast (Figure 2d). Cameras 1 and 5 correspond to longshore oriented
90 cameras with the highest azimuth angle with respect to shore normal ($|Az|$> 70 ° in Table 1), while camera
91 2, 3 and 4 are pointing the sea in a more cross-shore direction ($|Az|$< 45 ° in Table 1). Cameras are
92 mounted at different positions and heights on the mast (x0, y0 and z0 in Table 1); tilt and roll angles are
93 very different depending on cameras orientation.

94

95 **3. Materials and methods**

96 3.1. Camera geometry data

97 For approximatively 5 years (from April 2011 to April 2016), manual geometry solutions (tilt, roll and
98 azimuth angle) have been determined at the Sète station. Geometry solutions have been tediously obtained
99 using Argus toolbox (Holland et al., 1997) by clicking a certain number of fixed salient points on a large
100 amount of images from each of the 5 cameras. Geometry images have been processed approximatively
101 every 15 days and during storms at various times of the day for each camera to extract
102 shoreline/sandbar(s) position for other studies (Balouin et al., 2013; Bouvier et al., 2017). Over 2000
103 geometry solutions have been computed, that is, approximately 400 for each camera. The accuracy of such

104 a technique is difficult to generalize but Holman and Stanley (Holman and Stanley, 2007) estimated a $\pm$ 2
105 pixel accuracy for a wide-angle camera in a well-managed system. However, considering the large amount
106 of data at Sète and the fact that different operators performed the manual geometry solutions throughout
107 the years, we estimate that the accuracy of our geometry database is approximatively $\pm$ 5 pixels. Taking
108 into account the longshore resolution of the system (dy = 3 m at 500 m from the mast), we estimate the
109 mean accuracy of the geometry parameters (ΔD) to be approximately $\pm$ 0.1 ° for our entire database.
110 Figure 3 shows the evolution of the geometry solutions obtained for camera C5. Even if the confidence
111 limit of each solution is within $\pm$ 0.1 °, large tilt and roll variations (up to 1°) are observed. Only the
112 azimuth angle remains relatively constant and will therefore be considered hereafter as a non-variant
113 geometry parameter. It is important to note that the time variability in geometry parameters can consists in
114 abrupt changes (near august 2015, thick black cross in Figure 3) due to an occasional update of the basic
115 geometry solution induced during manual intervention on the camera system. Tilt and roll anomalies were
116 computed for each camera by subtracting the average tilt or roll solution (red curve in Figure 3) until a
117 jump occurs and that a new averaged solution appeared.
118 Tilt and roll anomaly will be given in degrees as real-world coordinate errors vary spatially. Camera
119 deviations anomaly systematically induces an error in pixels real-world location potentially reaching few
120 hundred meters far from the camera, depending on the grazing angle and lens properties. The induced
121 error (Err) can be approximated using classical trigonometry formulation:

$$\tan(\alpha_{Err}) = \frac{\overline{z0}}{L+Err} - \frac{\overline{z0}}{L}, \quad (1)$$

122 with α_{Err} *(°)* the camera deviation anomaly, *z0* (m) the height at which the video system is installed and *L*
123 (m) the horizontal distance of the sampling area from the camera. Figure 4 provides the estimated geo-
124 rectification induced error according to the distance from the camera and camera viewing angle deviation.
125 Depending on camera viewing angle anomaly, the estimated geo-rectification error can reach dramatic
126 values (Err>50 m for |α_Err |>0.25°) when the camera is located approximately 200 m from the sampling
127 area, which is a common video monitoring distance.

128

129 3.2. Environmental condition

130 3.2.1. Meteorological data

131 Specific environmental conditions are assumed to control changes in camera orientation. To verify this
132 hypothesis air temperature (T_{meteo}) and wind condition (velocity and direction) measured every hour by a
133 Meteo France station located a few kilometers away from the video station were collected. The 5-year
134 time series of the longshore and cross-shore wind components (V_l and V_c respectively) were computed
135 hourly. Nebulosity (N_{meteo}) which is a proxy of the percentage of the cloud cover was observed every 3
136 hours as an integer variable 0 (no cloud) to 8 (cloudy). An observer assessed the description of the state of
137 the sky according to the criteria most frequently adopted. Nebulosity is then linearly interpolated every
138 hour. Using these parameters, each camera geometry data (tilt and roll) was linked to a set of
139 environmental data.

140

141 3.2.2. Solar position

142 Structure deformation can occur as a result of thermal dilatation caused by solar absorption (Assem,
143 2011). To assess these effects, solar position was used as a proxy of solar absorption as it indicates the
144 exact position of the sun (Figure 5). Solar azimuth and elevation angle (ϕ_s and α_s respectively) were
145 computed for each camera geometry data according to (Reda and Andreas, 2004):

$$\phi_s = Arctan2\left(\frac{sinH'}{cosH'.sin\emptyset - tan\delta'.cos\emptyset}\right), \quad (2)$$

$$\alpha_s = 90 - \emptyset, \quad (3)$$

146 with the local hour angle (H'), sun declination (δ') and zenith angle $\emptyset$ observed from a particular point on
147 the Earth surface (here the head of the pole where cameras are mounted). The date and the local
148 coordinates (longitude, latitude and elevation) are needed. Solar azimuth angle varies from -180 ° to 180 °,
149 and is negative and positive when the sun is located eastward and westward, respectively. As is, the sun
150 rises approximatively to the east ($\phi \sim$ - 90 °) and sets to the west ($\phi \sim$ + 90 °) passing through the south
151 (ϕ = 0 °). The solar elevation angle is the altitude of the sun, that is, the angle between the horizon and the

center of the sun's disc.

3.3. Camera deviation models

3.3.1. Models construction

Given that camera geometry data is highly variable in time, identifying the preferred timescale(s) of geometry changes is complex. Despite the extensive data set used for training, the application of Artificial Neuronal Network (ANNs) was disregarded. The two primary reasons are that ANNs hamper the physical interpretation of the results and they typically provide unreliable prediction beyond the range represented by the training dataset. Robust methods such as based on Principal Component Analysis were also disregarded as they would lead to the loss of any cause-effect relationship between each variable. On the contrary, a 3rd degree polynomial regression model provides a unique value of regression coefficients, a moderate flexibility of shape, interpretable results and makes possible interactions between dependent variables. Such models were computed with multiple explanatory parameters (see eq. 4 and 5 below) and processed separately as a function of the observed camera tilt and roll angle deviation ($T_{Obs_{Az}}$ and $R_{Obs_{Az}}$ respectively). $F1_{az}$ and $F2_{az}$ correspond to the tilt and roll polynomial regression equations with $\varepsilon1_{az}$ and $\varepsilon2_{az}$ the associated error of the least square method. The index Az indicates the average azimuth angle of each camera with respect to shore normal:

$$T_{Obs_{Az}} = F1_{az}\,(\phi_s, \alpha_s, T_{meteo}, N_{meteo}, V_c, V_l) + \varepsilon1_{az}, \tag{4}$$

$$R_{Obs_{Az}} = F2_{az}\,(\phi_s, \alpha_s, T_{meteo}, N_{meteo}, V_c, V_l) + \varepsilon2_{az}, \tag{5}$$

To objectively assess model skill, linear squared-correlation (R^2) and root mean square error (RMSE) between the observed ($T_{Obs_{Az}}$ or $R_{Obs_{Az}}$) and simulated ($T_{Sim_{Az}}$ or $R_{Sim_{Az}}$) camera deviations have been computed. Then to consider measurement error (ΔD in section 3.1), the Brier Skill Score (BSS) has been computed for each model according to (Davidson et al., 2013).

$$BSS = 1 - \frac{\Sigma\left|\left|D_{Obs_{Az}} - D_{Sim_{Az}}\right| - \Delta D\right|^2}{\Sigma(D_{Obs_{Az}} - Db)^2}, \tag{6}$$

with $D_{Obs_{Az}}$ and $D_{Sim_{Az}}$ the angle deviation observed and simulated respectively. This method compares

174 the model residuals with a suitable baseline (Db). The choice of baseline has been fixed to zero as the
175 variable measured is an anomaly. Positive BSS indicates a significant improvement relative to the base
176 line with a value in excess of 0.0, 0.3, 0.6, 0.8 typically described respectively as 'poor', 'fair', 'good' and
177 'excellent' (Davidson et al., 2013).
178
179 3.3.2. Models' application and sensitivity
180 To assess the performance of our method, tilt and roll models have been run for camera C1 (second
181 worst model skill; see section 4.1) throughout the 22th of June 2013 (hindcast) and during a one-year non-
182 trained period starting on April 2016 (forecast). During that period, tilt and roll simulations were
183 compared with more than 50 manually computed geometry solutions (more details in section 3.1).
184 Finally, in order to determine equations' sensitivity on each of the 6 explanatory variables ($F1_{az}$ and
185 $F2_{az}$), each model has been processed on most possible cases. To reduce the computational time, each
186 variable has been decomposed into (10 by 1) vectors, resulting in 10^5 simulations for one variable tested.
187 Each vector boundary was defined by the percentile 10 and 90 of the variable intensity observed along the
188 study period. Model sensitivity was estimated for each equation $F1_{az}$ and $F2_{az}$ separately by averaging
189 the absolute value of the simulated tilt and roll anomaly along the dynamic variable.
190
191 **4. Results**
192 4.1. Models performance
193 Figure 6 shows the fit of the tilt and roll anomaly models for each of the 5 cameras ($T_{Obs_{Az}}$ and $R_{Obs_{Az}}$
194 versus $T_{Sim_{Az}}$ and $R_{Sim_{Az}}$). Camera viewing angle deviation models were found to significantly reproduce
195 the tilt and roll variability along the study period (from April 2011 to April 2016). Brier Skill Score (BSS)
196 indicates that models were rated as 'excellent' (BSS = 0.87). Root mean square error (RMSE) is relatively
197 small compared to the range of variations simulated ($\approx 60\%$ of the observed tilt and roll anomalies is
198 greater than the 0.12° RMSE). Furthermore, RMSE remains slightly higher than the estimated $\pm$ 0.1°

199 geometry accuracy (dashed lines in Figure 6) which suggests a good performance of the polynomial
200 regression models. Coefficient of determination (R^2) reveals that our method explains on average 71% of
201 the camera viewing angle deviation variability.

202 Details of the polynomial regression are provided for each models in Table 2. Statistical measurement
203 of the tilt and roll models have been realized for each camera separately. Results indicate that model
204 quality remains homogenous except for the roll anomaly on camera 5 ($F2_{-72}$). Even if BSS score is
205 relatively high (0.74), the coefficient of determination (R^2) is weak and RMSE remains high (0.19°). It is
206 suspected that the inaccuracy of the $F2_{-72}$ model is highly related to the quality of the roll angle
207 observations. Roll angle was relatively difficult to obtain precisely for this camera because of the practical
208 difficulty to identify ground control points resulting in errors on the roll anomaly values and the
209 inaccuracy of the $F2_{-72}$ model.

210

211 4.2. Model application

212 To assess the performance of our method, tilt and roll models have been run throughout the 22th of
213 June 2013 and during a one-year non-trained period starting on April 2016. We choose for this test the
214 second worst model skill ($F1_{80}$ and $F2_{80}$) used to reproduce the camera C1 variability (see Table 2).

215

216 4.2.1. One-day application

217 The 22th of June 2013 has been presented in the introduction as a day with high camera tilt and roll
218 variability (Figure 1). Inputs of the model are presented in Figures 7a, b and c. Elevation and azimuth
219 angle of the sun varied respectively from 0 to 70 ° and -150 to 150 ° during the day. Nebulosity was very
220 low (no clouds) and remained nearly the same while air temperature slightly increased until 15h00 UTC.
221 The coast was exposed to a reasonably constant offshore wind from NW during the entire day (-3.83 m/s
222 and -1.44 m/s on average for the cross-shore and longshore component respectively).

223 Tilt and roll anomaly varied approximately from -0.2° to 0.4° (Figures 7d and e). Even if direct
224 correlation with model inputs (Figure 7a-c) is readily difficult to identify, both models reproduce the

observed camera viewing angle anomaly with fair accuracy. Considering the estimated geometry accuracy, root mean square error is low (RMSE < 0.1°) and coefficient of determination is good (R^2 > 0.76) for both models. We suspect that the deviations from the observed roll anomaly could be due to an inaccurate ground control point manual detection when processing the camera geometry ($R_{Obs_{80}}$ in Figure 7e).

4.2.2. One-year application

Even if the first objective of the model presented was primarily more to better identify the primary environmental parameters controlling camera shifts, a comparison between manually resolved camera viewing angle deviations and model estimations is given Figure 8. The model was applied to a one-year non-trained period for camera 1 providing the estimated camera viewing angle deviation. The comparison between observed and simulated tilt and roll anomalies (Figure 8d and e) shows less accuracy than in Figure 7 with a root-mean square error reaching 0.15 ° in roll anomaly. However, solutions determined by the model significantly reduces the camera viewing angle anomaly and shows a good skill in prediction (BSS > 0.8). A conversion of the angle anomaly (°) into a real-coordinate error (m) provides additional into model improvement. For a 20-m high positioned camera, a 0.4° improvement of the camera viewing angle anomaly leads to a 100 m error correction in pixel position at a distance of 500 m from the camera (Figure 4).

4.3. Model sensitivity

To determine model sensitivity to each variable, each model has been run on all possible cases (section 3.3.2). The evolution of the simulated averaged absolute deviations ($\overline{|T_{Sim_{Az}}|}$ and $\overline{|R_{Sim_{Az}}|}$) are presented in Figure 9 for each model (different colors) as a function of variable evolution (different panels). When varying the solar azimuth angle or the nebulosity, the averaged deviation anomalies were strongly affected for all models (Figure 9a and c). These results suggest an important sensitivity of all models to both

variables. The value of the camera viewing angle deviation anomaly shows a dependency to the solar azimuth angle (ϕ_s) depending on camera orientation ($_{Az}$) on the mast (Figure 9a). Moreover, with low nebulosity (no clouds), we observe a large averaged deviation value for all models, and the contrary with intense nebulosity (Figure 9c). It is therefore deduced that low cloud cover is important to observe large tilt and roll variation. This behavior suggests that camera viewing angle deviations were linked to the deformation of the mast by solar absorption, which will be discussed in section 5. In contrast, the simulated deviations were less affected when varying other environmental parameters (Figures 9b, d, e, f).

To quantify the influence of each variable for all models, standard deviation of these curves have been computed. Results were averaged over all models and finally normalized across each variable. This parameter is presented as a sensitivity index (S_{Var}) in Table 3. Even if wind forcing is sometimes blamed for being responsible for camera deviation (Rutten et al., 2017; Vousdoukas et al., 2011), in the case of Sète, model sensitivity to longshore or cross-shore wind components remains very low (S_{Var} < 0.2 for both variables in Table 3). Air temperature and solar elevation angle do not affect significantly camera deviations neither with a S_{Var} of 0.1 and 0.16, respectively.

5. Discussion

Until recently, camera movements in fixed platform imagery for coastal application were largely ignored. Holman and Stanley (2007) introduced this difficulty highlighting that camera viewing angles regularly shift slightly for a variety of reasons including primarily thermal and wind effects, especially on tall towers. At the video monitoring system of Duck, North Carolina, camera viewing angle deviations can be described as a diurnal signal of about 2-pixel range, resulting in an approximately 30-m longshore drift, 1000 m away from the camera according to the pixel resolution of the video station. These deviations were only observed during sunny days, similar to our observations at Sète. Pear and Puleo (2009) also reported deviations of the video monitoring system at Rehoboth Beach, Delaware leading to important errors on the plan view image (estimated 500-m shift 2300 m from the camera). Similarly, Vousdoukas et al. (2011) observed cameras movement at the video system of Algarve, South Portugal introducing

276 significant geo-rectification errors.

277 Each time, the automatic correction methods consisted in determining the cameras viewing angle
278 deviation using a template matching method. Small, high-contrast regions (templates) from an original
279 base image are matched against corresponding locations in subsequent images, providing the missing
280 pinhole model extrinsic parameters (tilt, roll and azimuth). Such a technique requires a region of interest
281 selection in the camera view field consisting of fixed objects with distinct contrast. However, for many
282 coastal areas, this kind of pattern is not easily identified from camera images. Moreover, for scheduled
283 pixel time series acquisitions, users need to anticipate the camera shift to produce a well-referenced pixel
284 acquisition. Camera movements will not only induce the displacement of the area sampled, but also a
285 modification of the acquired pixel grid resolution. If not corrected, significant errors are introduced when
286 analyzing remotely-sensed hydrodynamic data such as longshore currents, run-up or wave celerity. At the
287 Sand Motor, a mega-scale beach nourishment in the Netherlands, Radermacher et al. (2018) observed
288 important errors in the remotely-sensed bathymetry depending on camera graze angles.

289 Therefore, it is crucial to define which environmental variables control those camera movements in
290 order to minimize these deviations for futures video system deployment. This will also help designing
291 appropriate data collection plan for which no deviation is suspected, which opens new perspectives to
292 develop generic methods for rectification procedures using time-varying geometry (Bergsma et al., 2014).
293 While the robustness of the polynomial regression inputs was questionable (not only measurement
294 accuracy but also the choice to simulate camera deviations as an instantaneous response to environmental
295 forcing), high skill was found for all models. Sensitivity analysis highlighted that all models are primarily
296 controlled by the solar azimuth angle and the nebulosity. While low cloud cover has been clearly
297 identified to systematically affect camera movements, processes connecting camera shifts with solar
298 azimuth angle remains misunderstood.

299 To fully understand which processes induce camera deviations, tilt and roll anomaly simulations
300 (Figure 10a and b respectively) are presented as a function of solar azimuth angle (ϕ_s) for each camera
301 orientation (Az) while others variables have been fixed (see the legend in Figure 10). The maximum

anomaly for C5 up to C1 occurs for progressively increasing solar azimuth angle. It is important to note that cameras C1 and C5, which are looking towards opposite direction (ENE and WSW, respectively), show very similar but out of phase deviations. Moreover, tilt and roll deviations patterns are clearly connected. For instance, a tilt deviation on a southward-looking camera (C3), is related with a roll deviation on an eastward- or westward-looking camera (C1 and C5). These results show that camera deviations are controlled by a local thermal deformation of the pole on which they are mounted. This process is induced by solar absorption of the face of the structure exposed to the sun leading to its dilatation. From structural mechanics, it is well known that temperature gradient across any cross section of a determined element (in this case the mast) produces changes of its curvature (Kassimali and Garcilazo, 2010). According to the theory, the mast will arc in the same direction of the temperature gradient, here from the enlighten face of the mast toward the opposite side. Instead of empirically modelling camera movements as if they were independent, one solution could be to determine directly the deformation of the pole where the camera are mounted depending of the environmental parameters, providing the camera viewing angle deviation for each camera. Technically, the solution is powerful but difficult to implement as it is highly influenced by the shape of the structure and the specific camera mount.

A major advantage of the model described in this study is to assess a complete time series of such camera movements at high frequency. While one specific day has been highlighted (section 4.2.1), model outputs also showed a certain seasonality. Lower anomalies amplitude is generally observed during the winter period (pinkish red dots in Figure 8d and e). This behavior could be explained by the cloud cover, generally higher in winter, which reduces sun action on the pole, resulting in lower changes in camera viewing angle. Although the model described in this study reproduced correctly the camera viewing angle deviation observed at Sète during the last 5 years, some errors on the prediction can occur when the environmental input data is not (or poorly) represented (very low temperature, high wind forces) during the model construction phase (polynomial regression). It is therefore anticipated that model skill increases with increasing amount, quality and range of training environmental data.

Conclusion

We showed that camera viewing angle deviations can induce large errors, with for instance more than 200 m and 20 m during a day in the longshore and cross-shore direction, respectively, at the video monitoring station of Sète. This correction remains sometimes difficult for seaward-looking camera and pixel time series because of the practical difficulty to identify ground control points. At the video monitoring station of Sète, cameras viewing angle deviations are controlled by thermal deformation of the pole where they are mounted. Deviation magnitude depends mainly on cloud cover, with a daily evolution due to camera orientation and solar azimuth angle. These deviations have been simulated using a polynomial regression method with good accuracy allowing a significant reduction of the geo-rectification errors. This method is applicable to other field sites subject to camera viewing angle anomaly. This study opens new perspectives in video monitoring, particularly to routinely improve camera geometry of video monitoring systems and to further derive higher quality remotely sensed hydrodynamic and morphological products.

Acknowledgements

The video system used in this work was funded by Thau Agglo and BRGM. CB acknowledges financial support from BRGM through a PhD grant. BC is funded by CHIPO (grant number ANR-14-ASTR-0004-01) supported by the Agence Nationale de la Recherche (ANR). L. Desbiendras, J. Tesson, R. Belon, M. Giusti, Y. Colombet, P-A. Picand, F. Longueville, A. Latapy, S. Hureau and M. Guebba are greatly acknowledged for their help in processing video data.

References

Aarninkhof, S.G.J., Turner, I.L., Dronkers, T.D.T., Caljouw, M., Nipius, L., 2003. A video-based technique for mapping intertidal beach bathymetry. Coast. Eng. https://doi.org/10.1016/S0378-3839(03)00064-4

Alexander, P.S., Holman, R.A., 2004. Quantification of nearshore morphology based on video imaging. Mar. Geol. 208, 101–111. https://doi.org/10.1016/j.margeo.2004.04.017

Almar, R., Castelle, B., Ruessink, B.G., Sénéchal, N., Bonneton, P., Marieu, V., 2010. Two- and three-dimensional double-sandbar system behaviour under intense wave forcing and a meso-macro tidal range. Cont. Shelf Res. https://doi.org/10.1016/j.csr.2010.02.001

Almar, R., Cienfuegos, R., Catalán, P.A., Michallet, H., Castelle, B., Bonneton, P., Marieu, V., 2012. A new breaking wave height direct estimator from video imagery. Coast. Eng. 61, 42–48. https://doi.org/10.1016/j.coastaleng.2011.12.004

Assem, E.O., 2011. Correlating thermal transmittance limits of walls and roofs to orientation and solar absorption. Energy Build. 43, 3173–3180. https://doi.org/10.1016/j.enbuild.2011.08.015

Balouin, Y., Tesson, J., Gervais, M., 2013. Cuspate shoreline relationship with nearshore bar dynamics during storm events – field observations at Sete beach, France. J. Coast. Res. 65, 440–445. https://doi.org/10.2112/SI65-075.1

Bergsma, E.W.J., Conley, D.C., Davidson, M.A., O'Hare, T.J., Holman, R.A., 2014. An Assesment Of Video-Based Bathymetry Estimation In A Macro-Tidal Environment. Coast. Eng. Proc. 34th Conf. Coast. Eng. 1–10.

Bouvier, C., Balouin, Y., Castelle, B., 2017. Video monitoring of sandbar-shoreline response to an offshore submerged structure at a microtidal beach. Geomorphology 295, 297–305. https://doi.org/10.1016/j.geomorph.2017.07.017

Chickadel, C.C., 2003. An optical technique for the measurement of longshore currents. J. Geophys. Res. 108, 3364. https://doi.org/10.1029/2003JC001774

Colomina, I., Molina, P., 2014. Unmanned aerial systems for photogrammetry and remote sensing: A review. ISPRS J. Photogramm. Remote Sens. 92, 79–97.

Davidson, M.A., Splinter, K.D., Turner, I.L., 2013. A simple equilibrium model for predicting shoreline change. Coast. Eng. 73, 191–202. https://doi.org/10.1016/j.coastaleng.2012.11.002

Faugeras, O., 1993. Three-dimensional computer vision: a geometric viewpoint, MIT PRESS. Cambridge, Massachusetts. https://doi.org/10.1007/978-3-642-82429-6_2

Gallop, S.L., Bryan, K.R., Coco, G., Stephens, S.A., 2011. Storm-driven changes in rip channel patterns on an embayed beach. Geomorphology 127, 179–188. https://doi.org/10.1016/j.geomorph.2010.12.014

Hartley, R., Zisserman, A., 2004. Multiple View Geometry in Computer Vision, 2nd ed, Cambridge UK Cambridge Univ Press.

Heikkila, J., Silven, O., 1997. A Four Step Camera Calibration Procedure within Implicit Image Correction. Comput. Vis. Pattern Recognition, proceedings; IEEE Comput. Soc. Conf. 1997 1106–1112.

Holland, K.T., Holman, R. a, Lippmann, T.C., Stanley, J., Plant, N., 1997. Practical Use of Video Imagery in Nearshore Oceanographic Field Studies - Oceanic Engineering, IEEE Journal of. IEEE J. Ocean. Eng. 22, 81–92.

Holland, K.T., Raubenheimer, B., Guza, R.T., Holman, R.A., 1995. Runup kinematics on a natural beach. J. Geophys. Res. 100, 4985. https://doi.org/10.1029/94JC02664

Holman, R., Plant, N., Holland, T., 2013. CBathy: A robust algorithm for estimating nearshore bathymetry. J. Geophys. Res. Ocean. https://doi.org/10.1002/jgrc.20199

Holman, R.A., Guza, R.T., 1984. Measuring run-up on a natural beach. Coast. Eng. 8, 129–140. https://doi.org/10.1016/0378-3839(84)90008-5

Holman, R.A., Stanley, J., 2007. The history and technical capabilities of Argus. Coast. Eng. https://doi.org/10.1016/j.coastaleng.2007.01.003

Holman, R.A., Symonds, G., Thornton, E.B., Ranasinghe, R., 2006. Rip spacing and persistence on an embayed beach. J. Geophys. Res. Ocean. 111, 1–17. https://doi.org/10.1029/2005JC002965

Kassimali, A., Garcilazo, J.J., 2010. Geometrically Nonlinear Analysis of Plane Frames Subjected to Temperature Changes. J. Struct. Eng. 136, 1342–1349. https://doi.org/10.1061/(ASCE)ST.1943-541X.0000233

Larson, M., Kraus, N.C., 1994. Temporal and spatial scales of beach profile change, Duck, North Carolina. Mar. Geol. 117, 75–94. https://doi.org/10.1016/0025-3227(94)90007-8

Lippmann, T.C., Holman, R.A., 1991. Phase Speed and Angle of Breaking Waves Measured with Video Techniques, in: Coastal Sediments (1991). pp. 542–556.

Lippmann, T.C., Holman, R.A., 1989. Quantification of sand bar morphology: A video technique based on wave dissipation. J. Geophys. Res. 94, 995. https://doi.org/10.1029/JC094iC01p00995

Lippmann, T.C., Smith, G.M., 2009. Shallow Surveying in Hazardous Waters. US Hydrogr. Conf. 2009 1–12.

Osorio, A.F., Medina, R., Gonzalez, M., 2012. An algorithm for the measurement of shoreline and intertidal beach profiles using video imagery: PSDM. Comput. Geosci. 46, 196–207. https://doi.org/10.1016/j.cageo.2011.12.008

Pearre, N.S., Puleo, J.A., 2009. Quantifying Seasonal Shoreline Variability at Rehoboth Beach, Delaware, Using Automated Imaging Techniques. J. Coast. Res. 254, 900–914. https://doi.org/10.2112/08-1029.1

Pérez Muñoz, J.C., Ortiz Alarcón, C.A., Osorio, A.F., Mejía, C.E., Medina, R., 2013. Environmental applications of camera images calibrated by means of the Levenberg-Marquardt method. Comput. Geosci. 51, 74–82. https://doi.org/10.1016/j.cageo.2012.07.016

Radermacher, M., de Schipper, M.A., Reniers, A.J.H.M., 2018. Sensitivity of rip current forecasts to errors in remotely-sensed bathymetry. Coast. Eng. 135, 66–76. https://doi.org/10.1016/j.coastaleng.2018.01.007

Reda, I., Andreas, A., 2004. Solar position algorithm for solar radiation applications. Sol. Energy 76, 577–589. https://doi.org/10.1016/j.solener.2003.12.003

Ruessink, B.G., Pape, L., Turner, I.L., 2009. Daily to interannual cross-shore sandbar migration: Observations from a multiple sandbar system. Cont. Shelf Res. https://doi.org/10.1016/j.csr.2009.05.011

Rutten, J., Ruessink, B.G., Price, T.D., 2017. Observations on sandbar behaviour along a man-made curved coast. EARTH Surf. Process. LANDFORMS Earth Surf. Process. Landforms. https://doi.org/10.1002/esp.4158

Turner, I.L., Harley, M.D., Drummond, C.D., 2016. UAVs for coastal surveying. Coast. Eng. 114, 19–24. https://doi.org/10.1016/j.coastaleng.2016.03.011

Vousdoukas, M.I., Ferreira, P.M., Almeida, L.P., Dodet, G., Psaros, F., Andriolo, U., Taborda, R., Silva, A.N., Ruano, A., Ferreira, Ó.M., 2011. Performance of intertidal topography video monitoring of a meso-tidal reflective beach in South Portugal. Ocean Dyn. 61, 1521–1540. https://doi.org/10.1007/s10236-011-0440-5

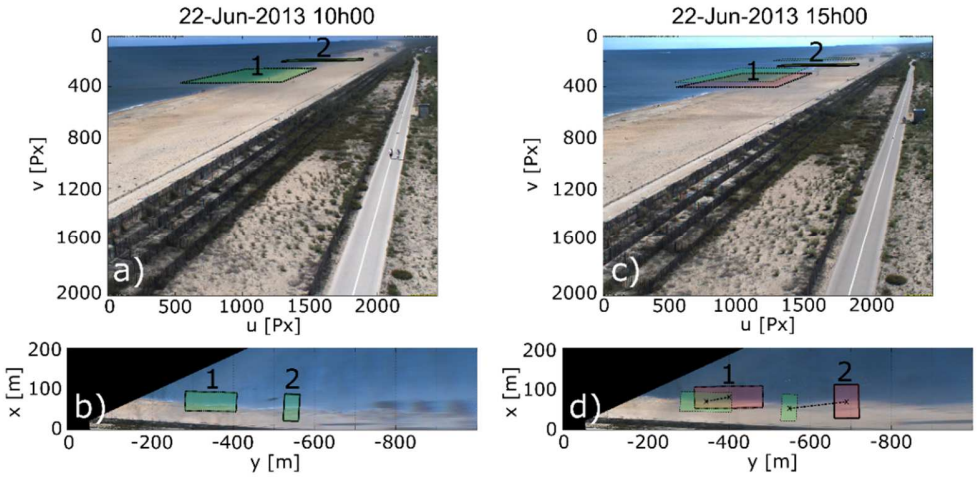

Figure 1. a) Argus images captured on June 22, 2013 at 10h00 UTC at the beach of Sète (France). b) Associated rectified image with location of two schematic sampling areas (green boxes). Panels c) and d) highlight the impact of camera viewing angle deviation with an image captured a few hours after (at 15h00 UTC) by the same camera.

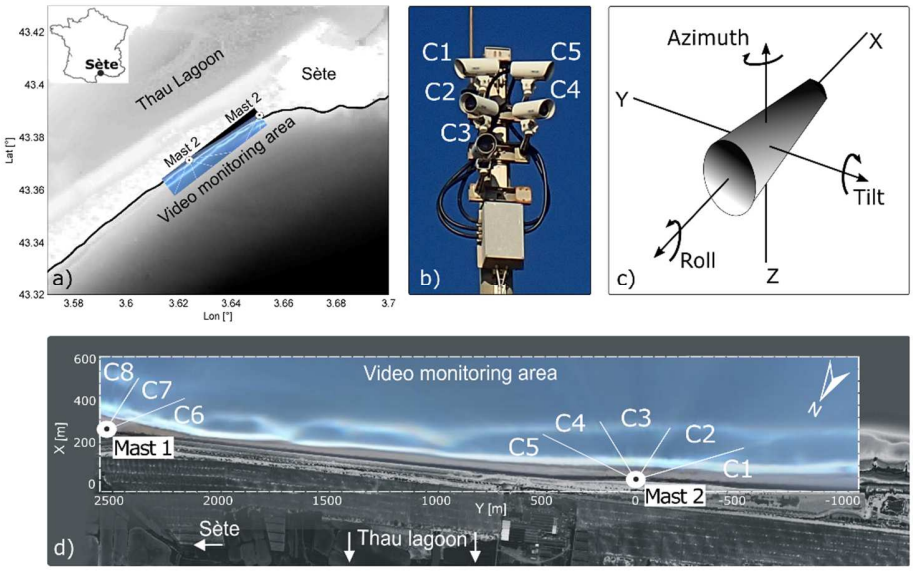

Figure 2. a) Study site with the location of the video monitoring area. Photography of the video monitoring system deployed at the beach of Sète. Geometry parameters (tilt, roll and azimuth) required for image rectification. Rectified plan view timex images (23 Oct 2011) with indication of the camera fields.

Table 1. Original geometry parameters for cameras mounted on mast 2 at the station of Sète.

N° Camera	Tilt [°]	Roll [°]	*Az* [°]	x0 [m]	y0 [m]	z0 [m]
1	78.41	-1.16	79.65	-0.05	0.25	20.42
2	75.20	-2.33	43.90	0.01	0.24	20.10
3	72.87	-3.58	-1.04	0.05	0.31	19.76
4	74.47	1.50	-38.13	-0.01	0.72	20.11
5	80.62	-0.51	-72.27	-0.02	0.75	20.41

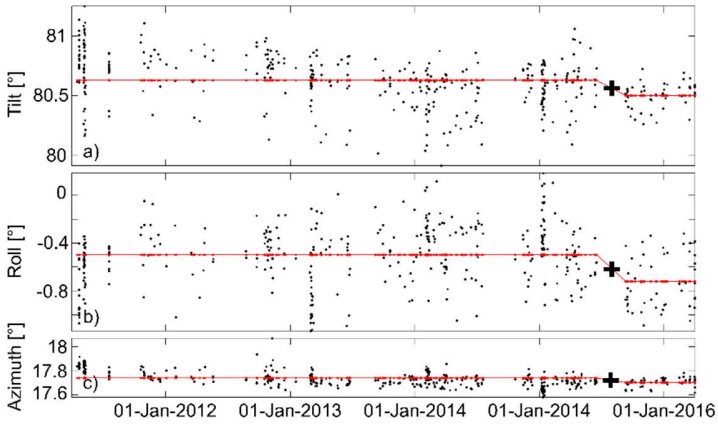

Figure 3. Time series of geometry solutions for the a) tilt, b) roll and c) azimuth angle of camera C5 at the video monitoring station of Sète. The jump indicated by a black cross corresponds to a slight reset of camera aim. Red line represents the average solution for a non-reset period.

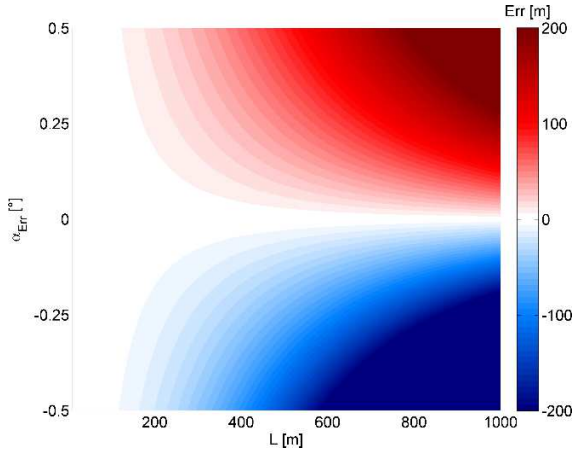

Figure 4. Estimated geo-rectification errors (Err) depending of the distance from camera to monitored area (L) and of the viewing angle deviation (α_{Err}) for a camera mounted at a 20-m high.

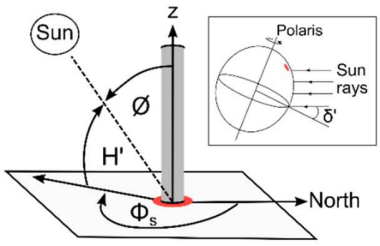

Figure 5. The position of the Sun in the sky is a function of both the time and the geographic location of observation on Earth's surface.

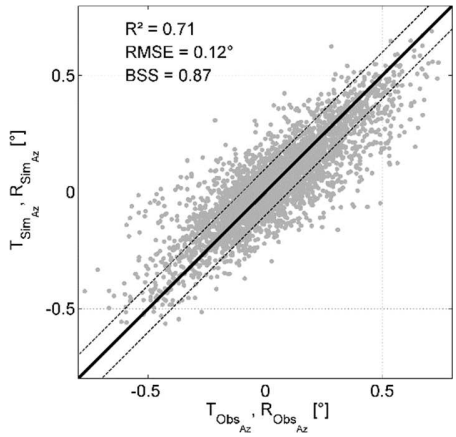

Figure 6. Model predictions ($\boldsymbol{T_{Sim_{Az}}}$ and $\boldsymbol{R_{Sim_{Az}}}$) versus observations ($\boldsymbol{T_{Obs_{Az}}}$ and $\boldsymbol{R_{Obs_{Az}}}$). The solid line is the linear function $\boldsymbol{f(x) = y}$. Dashed lines represent the estimated geometry accuracy interval $\boldsymbol{f(x) = y \pm 0.1}$.

Table 2. Results of the 3rd degree polynomial regression models.

	$\boldsymbol{F1_{az}}$			$\boldsymbol{F2_{az}}$		
N° Camera	R^2	RMSE [°]	BSS	R^2	RMSE [°]	BSS
C1 (az = 80°)	0.74	0.08	0.84	0.61	0.12	0.84
C2 (az = 44°)	0.80	0.07	0.86	0.78	0.11	0.90
C3 (az = -1°)	0.77	0.09	0.88	0.76	0.12	0.92
C4 (az = -38°)	0.84	0.08	0.90	0.66	0.14	0.88
C5 (az = -72°)	0.77	0.10	0.91	0.38	0.19	0.74

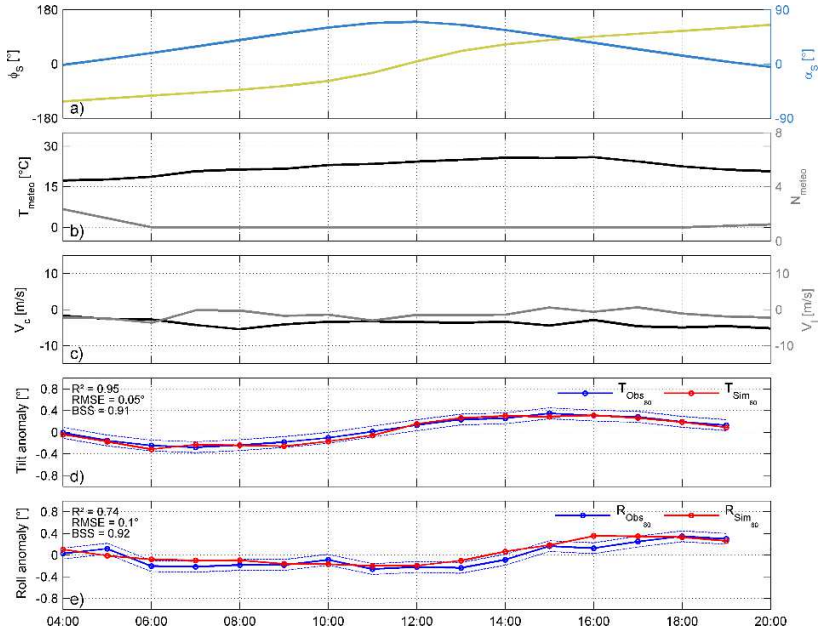

Figure 7. Tilt and roll anomaly forecast for camera 1 during the 22th of June 2013. Panels a), b) and c) present the model inputs with respectively, the position of the sun (ϕ_s, $\boldsymbol{\alpha_s}$), weather condition (T_{meteo}, N_{meteo}) and wind velocity (V_c, V_l). Panels d) and e) illustrate tilt and roll anomaly outputs (pinkish red dots) and also provide a comparison between modeled (red dots on thick curve) and observed (blue dots on thick curve) camera viewing angle deviation.

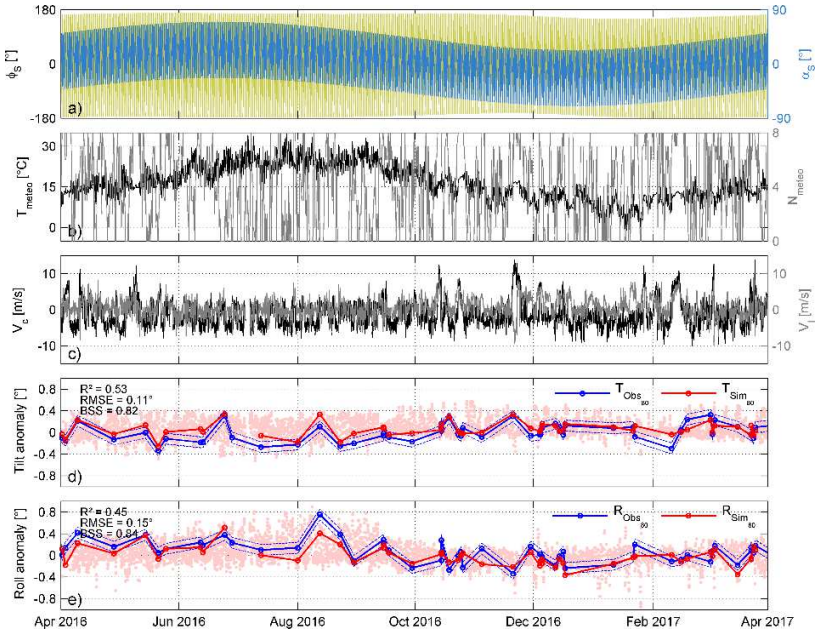

Figure 8. Tilt and roll anomaly forecast for camera 1 during a one year period from April 2016. Panels a), b) and c) present the model inputs with respectively, the position of the sun (ϕ_s, $\boldsymbol{\alpha_s}$), weather condition (T_{meteo}, N_{meteo}) and wind velocity (V_c, V_l). Panels d) and e) illustrate tilt and roll anomaly outputs (pinkish red dots) and also provide a comparison between modeled (red dots on thick curve) and observed (blue dots on thick curve) camera viewing angle deviation.

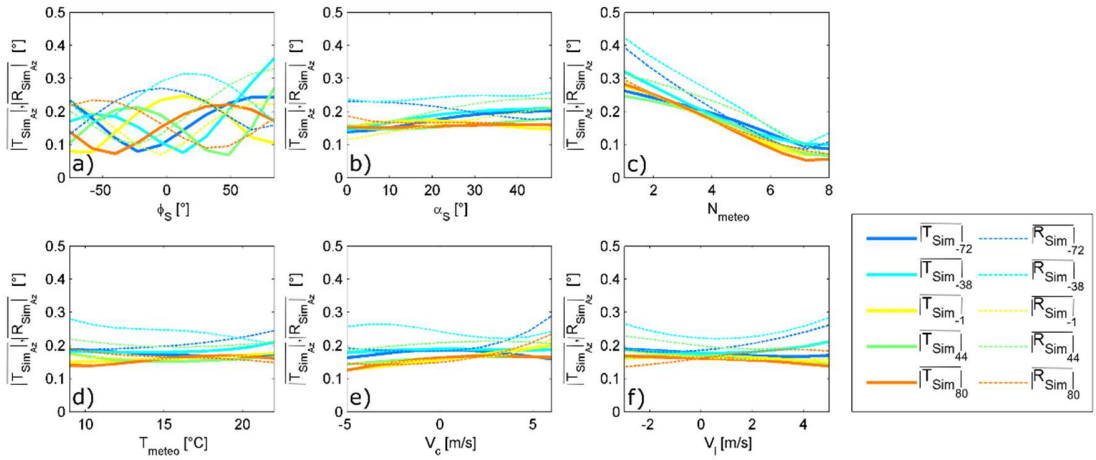

Figure 9. a) to f) Model sensitivity to each variable. Simulated averaged absolute tilt ($\boldsymbol{T_{Sim_{Az}}}$) and roll ($\boldsymbol{R_{Sim_{Az}}}$) deviation computed along each environmental variable (different panel) and presented for each model (different colors).

Table 3. Model sensitivity index $\boldsymbol{S_{Var}}$ to all environmental variables.

Variable	ϕ_s	α_s	$\boldsymbol{N_{meteo}}$	T_{meteo}	V_c	V_l
S_{Var}	**0.58**	0.16	**0.76**	0.10	0.16	0.13

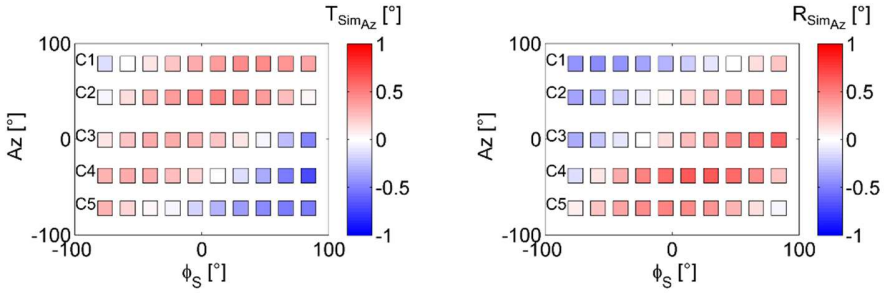

Figure 10. Simulation of the tilt and roll anomaly ($\boldsymbol{T_{Sim_{Az}}}$, $\boldsymbol{R_{Sim_{Az}}}$ in a) and b), respectively) as a function of solar and camera azimuth angle (ϕ_s and Az respectively). For each simulation, nebulosity has been set to 1, solar elevation angle to 21°, temperature to 15°C and cross-shore/longshore wind component to 0 m/s.